First-principles study of electron and hole doping effects in perovskite nickelates

Lucia Iglesias,[1] Manuel Bibes,[1] and Julien Varignon[2]

[1]*Unité Mixte de Physique, CNRS, Thales, Université Paris Sud, Université Paris-Saclay, F-91767 Palaiseau, France*

[2]*Laboratoire CRISMAT, CNRS UMR 6508, ENSICAEN, Normandie Université, 6 boulevard Maréchal Juin, F-14050 Caen Cedex 4, France*

(Received 15 January 2021; revised 4 June 2021; accepted 23 June 2021; published 12 July 2021)

Rare-earth nickelates $R^{3+}Ni^{3+}O_3$ (R = Lu-Pr, Y) show a striking metal-insulator transition in their bulk phase whose temperature can be tuned by the rare-earth radius. These compounds are also the parent phases of the newly identified infinite layer $RNiO_2$ superconductors. Although intensive theoretical works have been devoted to understand the origin of the metal-insulator transition in the bulk, there have only been a few studies on the role of hole and electron doping by rare-earth substitutions in $RNiO_3$ materials. Using first-principles calculations based on density functional theory (DFT) we study the effect of hole and electron doping in a prototypical nickelate $SmNiO_3$. We perform calculations without Hubbard-like U potential on Ni $3d$ levels but with a meta–generalized gradient approximation better amending self-interaction errors. We find that at low doping, polarons form with intermediate localized states in the band gap resulting in a semiconducting behavior. At larger doping, the intermediate states spread more and more in the band gap until they merge either with the valence (hole doping) or the conduction (electron doping) band, ultimately resulting in a metallic state at 25% of R cation substitution. These results are reminiscent of experimental data available in the literature and demonstrate that DFT simulations without any empirical parameter are qualified for studying doping effects in correlated oxides and exploring the mechanisms underlying the superconducting phase of rare-earth nickelates.

DOI: 10.1103/PhysRevB.104.035123

I. INTRODUCTION

Transition metal oxide perovskites ABO_3, with a $3d$ element sitting on the B site, are an important class of materials that show a vast array of functionalities such as octahedra rotations, ferroelectricity, magnetism, or superconductivity, for instance [1]. Among these perovskites, rare-earth nickelates $R^{3+}Ni^{3+}O_3$ (R = Lu-Pr, Y) have attracted a lot of attention for several reasons [2,3]: (i) they exhibit a tunable metal-insulator transition as a function of the rare-earth size in their bulk form, (ii) they were proposed as magnetically induced ferroelectric compounds [4], and (iii) due to their proximity with Cu in the periodic table, they have been suggested to potentially show cupratelike superconductivity [5]. The triggering mechanism of the metal-insulator transition and the precise electronic structure of the insulating phase have been established recently [6–11]. They rely on an electronic instability associated with an unstable 3+ formal oxidation state on Ni cations that leads to charge and bond disproportionation: Ni sites split into apparent Ni^{2+} and Ni^{4+} cations, resulting in an alternative expansion/contraction of O_6 octahedra, the so-called breathing distortion [Fig. 1(a)]. The ability of nickelates to undergo disproportionation was moreover shown to be coupled to the octahedra rotation amplitude [6,7] [Fig. 1(b)], itself connected to the A-to-B cation size mismatch (i.e., Goldschmidt tolerance factor [12]). Although ligand holes exist in nickelates due to their negative charge transfer nature [8,13,14], cupratelike superconductivity in these compounds remained a dream for more than 30 years [5]. It is only in 2019 that superconductivity was finally achieved in nickelates through an appropriate chemical reduction to an infinite layer phase $RNiO_2$ and A site cation substitution resulting in hole doping [15,16]. Although the superconducting temperature ($\sim$15 K) remains relatively low with respect to that of the cuprates, this achievement offers an alternative playground to test our solid state theories of pairing mechanisms in correlated oxide superconductors [17].

The $RNiO_2$ phase has been widely studied theoretically since the discovery of superconductivity in 2019. However, there are actually very few studies on doping effects in the $RNiO_3$ perovskite phase, even though this phase is the starting point to achieve the infinite-layer superconducting phase. Electron doping effects through hydrogen insertion or oxygen vacancies have been studied [18–23], altering the metal-insulator transition and band gap amplitude, but the A site cation substitution has been less studied. Hole and electron doping through Ca or Sr and Th or Ce substitutions, respectively, have been studied experimentally in bulk and thin films of $NdNiO_3$ and $SmNiO_3$, revealing a decrease of the metal-insulator transition temperature for substitutions as large as 10% [24–26] or a metallic state at doping levels of 30% [27]. At the theoretical level, electronic calculations on trends in electronic and structural properties with substitution of A site cations are missing in the $RNiO_3$ family. Understanding polaron formation, the evolution of band gaps and lattice distortions upon doping in the ABO_3 phase is crucial for several reasons: (i) it may provide potential insights in the underlying superconducting $RNiO_2$ phase and/or (ii) we may benchmark our electronic structure calculations performed with DFT-no-U for studying doping effects in the parent $RNiO_3$ phase, to then transpose it to the reduced superconducting $RNiO_2$ phase. In this regard, previous studies shown that density functional theory (DFT) calculations

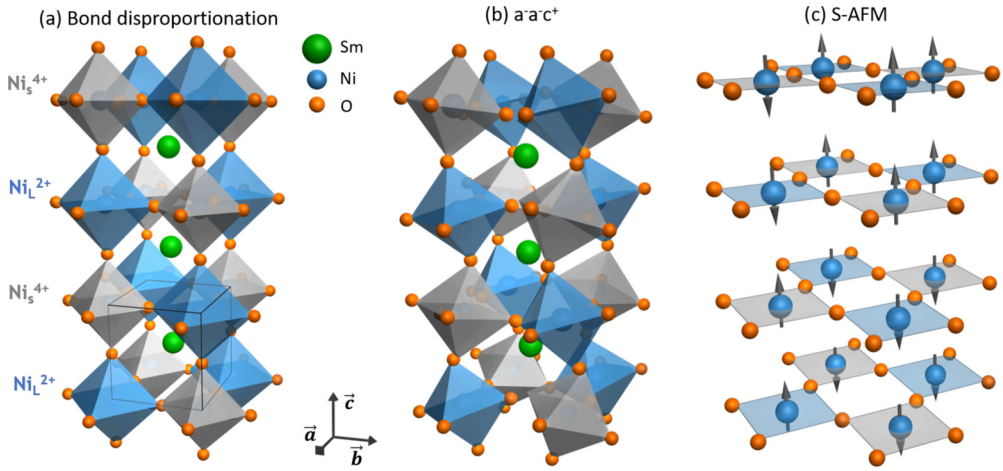

FIG. 1. (a) Sketch of the orthorhombic *Pbnm* structure showing the usual bond disproportionation B_{oc} producing a rocksalt pattern of Ni^{4+} (grey octahedra, Ni_S) and Ni^{2+} (blue octahedra, Ni_L) cations and (b) the $a^-a^-c^+$ rotation. (c) *S*-type antiferromagnetic structure used in the simulations.

involving the meta–generalized gradient approximation meta-GGA strongly constrained and appropriately normed (SCAN) [28] functional can successfully address the physics of bulk 3*d* transition metal ABO_3 compounds [29] without any empirical *U* parameter or the doping effects in the cuprates superconductor La_2CuO_4 [30,31].

In this paper, we inspect the role of electron and hole doping through Sm substitution in $SmNiO_3$ with first-principles calculations based on DFT without empirical *U* parameter. We find that at low hole or electron doping content, intermediate acceptor or donor states form in the band gap, producing a semiconducting state. Upon increasing the doping content, we observe that intermediate states spread more and more in the band gap until they merge with the valence or conduction band, resulting in a strong decrease of the band gap. This is further accompanied by a vanishing of the breathing mode distortion, hinting at the appearance of the metallic phase. Our DFT-no-*U* simulations, performed with the recent meta-GGA SCAN functional better amending self-interaction errors inherent to DFT, provide results consistent with experimental results available in the literature. This validates the use of the SCAN functional for studying doping effects in ABO_3 materials and the underlying mechanisms yielding superconductivity in correlated oxides.

II. METHOD

Technique. First-principles calculations are performed with density functional theory (DFT) using the Vienna *Ab initio* Simulation Package (VASP) [32,33]. In $RNiO_3$ materials, the band gap is strongly sensitive to the magnetic order [8] and since the low-temperature phase usually inherits the physics of the high temperature paramagnetic state [7], we employed the complex antiferromagnetic S (S-AFM) order appearing in the low temperature phase of bulk $SmNiO_3$. It consists of up-up-down-down spin chains in the (*ab*) plane with different stacking along the *c* axis [4] [see Fig. 1(c)]. No exploration of magnetic orders has been performed and it is left for possible future studies. The monoclinic $P2_1/n$ structure corresponding to a $(2\sqrt{2}a, \sqrt{2}a, 4a)$ unit cell (16 formula unit; *a* is the primitive cubic cell lattice parameter) allowing for the complex AFM-S order as well as disproportionation effects is used for all simulations [sketched in Fig. 1(a)]. The cutoff energy is set to 500 eV along with a $3 \times 6 \times 2$ Gamma centered K mesh and the convergence criterion for the total energy is fixed to 10^{-4} meV. Self-consistent field (SCF) cycles are converged until energy difference is lower than 10^{-7} eV between consecutive steps. Projected augmented wave (PAW) potentials [34] without treating explicitly *4f* electrons for Sm and *p* electrons for Ni cations were used in the simulations. For Ce doping, we have used the Ce PAW potentials containing *4f* electrons. Full geometry optimizations (atomic positions + lattice parameters) are performed until forces acting on each atom are lower than 0.05 eV/Å for bulk and doped compounds. Finally, the amplitude of lattice distortions appearing in the identified ground states are extracted using symmetry mode analysis with ISOTROPY applications [35,36].

Choice of the exchange-correlation functional. While it is often believed that more complex techniques than DFT (e.g., dynamical mean field theory) are required to describe the physics of correlated oxides, we recently showed that, even without any empirical *U* potential on Ni 3*d* levels, DFT can provide a fine description of the physics of transition metal oxide ABO_3 perovskites [7,29]. This is possible if one properly includes all degrees of freedom (symmetry lowering events, charge and spin orders, different local motifs) in the simulations. One must also involve an exchange-correlation functional properly correcting self-interaction errors inherent to DFT, thus it is necessary to go beyond standard local density approximation (LDA) or generalized gradient approximation (GGA) functionals. We have used the meta-GGA SCAN functional with no *U* parameter [28], previously shown to be suited for $YNiO_3$ [29]. DFT simulations have previously revealed the electronic structure of the insulating phase of nickelates and enabled a deep understanding of the mechanism producing the metal-insulator phase transition [7,8,29,37]. Results with the common PBEsol + *U* method are provided in Appendix C for comparison.

Improvement of SCAN functional over classical LDA or GGA functionals for the band gap description. The band gap of a material is a fundamental quantity at the core of several applications such as catalysis, photovoltaics, or switching of ferroelectrics [38]. It also quantifies the ability of a compound to host intermediate states in the band gap. Thus, reproducing a band gap amplitude with our DFT simulations that is compatible with experiments is of general relevance. The fundamental band gap E_g^f of a material is defined as the ground state energies E difference between the $N+1$ and N-1 electronic systems and the N electronic systems, i.e., $E_g^f = E(N+1) + E(N\text{-}1) - 2E(N)$. Within the exact Kohn-Sham theory, the Kahn-Sham band gap E_g^{KS} is given by the eigenvalues of the conduction band minimum (CBM) and valence band maximum (VBM), i.e., $E_g^{KS} = E_{CBM} - E_{VBM}$. E_g^f and E_g^{KS} are not equal and the connection between the two quantities is related to the exchange-correlation discontinuity Δ_{xc} : $E_g^f = E_g^{KS} + \Delta_{xc}$. DFT functionals such as local density approximation (LDA) or generalized-gradient approximation (GGA) lack a derivative discontinuity ($\Delta_{xc} = 0$) and hence it yields the famous band gap underestimation from DFT [39]. More sophisticated functionals such as hybrid involve a derivative discontinuity and thus offer a better description of band gaps.

Instead, some functionals are implemented within the generalized Kohn-Sham (gKS) scheme [40], in which the exchange-correlation potential is orbital dependent and thus is nonlocal. Within this framework, it was demonstrated by Perdew *et al.* that the gKS band gap E_g^{gKS} is equal to the fundamental gap E_g^f (Ref. [41]), despite the possible lack of a derivative discontinuity Δ_{xc}. The SCAN functional [28] falls with the gKS implementation and indeed provides a fair description of band gaps in cuprates [30,31] and transition metal perovskite oxides [29] or optical data of cuprates and nickelates [42]. Thus assessing the ability of SCAN functional in studying doping effects in oxides is a valuable addition to the community.

Improvement of SCAN over DFT+U for studying doping effects. Upon electron or hole doping a transition metal (TM) oxide perovskite, the formal d electron count varies and thus there is no guarantee that the U potential acting on $3d$ elements should be constant for inequivalent TM sites in the DFT + U method. For instance, electronic properties of isovalent $3d^1$ perovskites such as $YTiO_3$ and $CaVO_3$ or $3d^1$ and $3d^2$ perovskites such as $YTiO_3$ and YVO_3 are properly reproduced with DFT + U for U a potential of 2.5, 1.25, and 3.5 eV, respectively [7,43,44]. Therefore, the ability to study doping effects without relying on any empirical parameters is a significant advance to explore potential polaron formation/localization of intermediate states in the band gap.

Method to describe doping effects. A site cation substitution is modeled within the ($2\sqrt{2}a$, $\sqrt{2}$ a, $4a$) unit cell (16 formula unit with respect to the primitive cubic cell) with atomic position obtained using the special quasirandom structure (SQS) method [45] implemented in the ATAT package [46], which allows us to extract within a given supercell the configuration maximizing the disorder characteristic of an alloy. The choice of such a supercell is ruled by several constraints: (i) the cell has to allow structural distortions such as octahedra rotations or bond disproportionation; (ii) it has to accommodate the S-AFM order, and (iii) simulations have to remain feasible since doping breaks all symmetries, the compound being in a $P1$ cell for all doping contents. Hole (electron) doping is achieved by replacing Sm^{3+} with Ca^{2+} (hole doping) or Ce^{4+} (electron doping) and within our supercell size, one thus accesses doping contents by steps of 6.25%. We provide in Appendix A the A site cation positions corresponding to the different doping content used in the simulations. Proper simulation of doping effects requires us to study polaron formation in the material. To that end, we have used the modified VASP routine to initially force orbital occupancy of transition metal d states with DFT + U [47]. Starting from the pristine material, we force the hole(s) or the electron(s) added to the system to localize on a precise Ni site in the vicinity of the substituted cations by fixing the e_g level occupancies. Then, we performed a few steps of structural relaxations without preserving the symmetry of the wave function before switching off the constraint and let the solver relax to the ground state with the SCAN-no-U functional.

TABLE I. Structural properties of our relaxed $SmNiO_3$ ground state with the SCAN functional. The identified space group is $P2_1/n$. Amplitudes (in Å per formula unit) of lattice distortions are also reported.

a (Å)	b (Å)	c (Å)	α (°)
5.4039	5.2997	7.5366	90.0305
	x/a	y/b	z/c
Sm	0.0511	0.5121	−0.0250
Ni	0	0	0
Ni	0	0	0.5000
O	0.4831	0.4179	−0.2567
O	0.2963	−0.2161	−0.4566
O	0.7830	−0.2977	−0.4552
	B_{oc} (Å/f.u.)	$a^-a^-c^0$ (Å/f.u.)	$a^0a^0c^+$ (Å/f.u.)
	0.0885	0.6476	0.4322

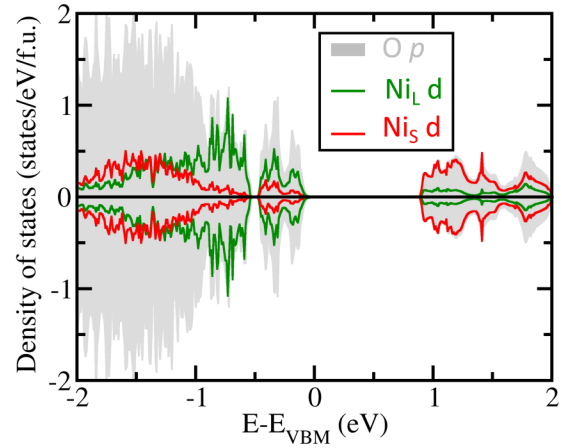

FIG. 2. Projected density of states (in states/eV/formula unit) on Ni_L d (green), Ni_S d (red), and O p (filled grey) states in the ground state structure of bulk $SmNiO_3$ using the SCAN exchange-correlation functional. The 0 energy is set at the valence band maximum.

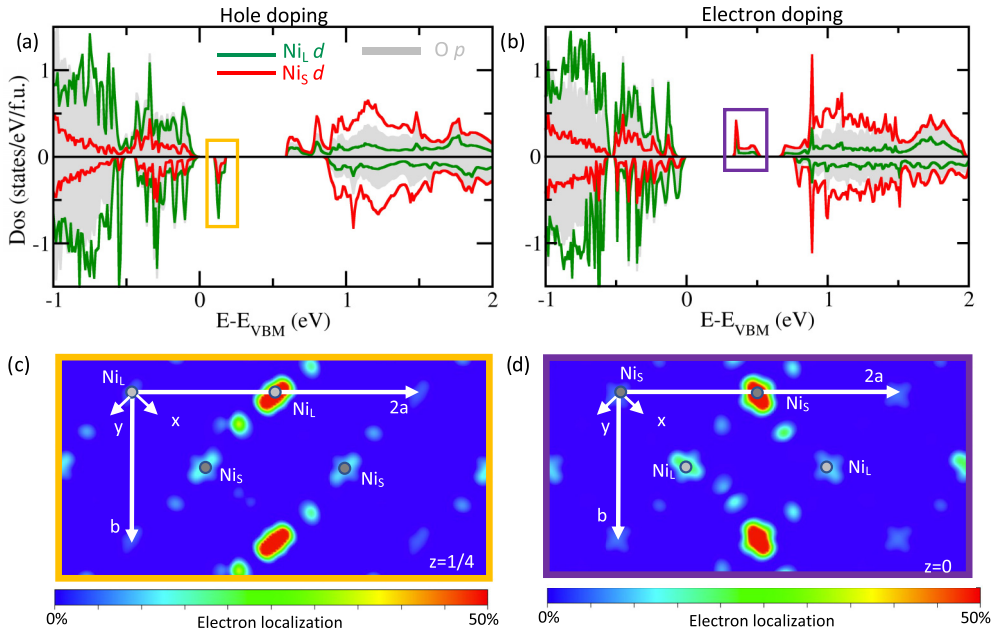

FIG. 3. (a),(b) Projected density of states on Ni$_L$ d (green), Ni$_S$ d (red), and O p (filled grey) states in hole (a) and electron (b) doped $SmNiO_3$ using SCAN functional. (c),(d) Wave function squared maps of electrons associated with the intermediate states observed for 6.25% hole (c) and electron (d) doped compounds. The 0 energy is set at the valence band maximum.

III. RESULTS

A. $SmNiO_3$ ground state electronic properties

We have first relaxed $SmNiO_3$ bulk material with the SCAN functional. Consistently with previous DFT studies [6–8], the monoclinic $P2_1/n$ cell is stabilized in our simulations. Lattice parameters and atomic positions are reported in Table I. We also report in Table I the amplitudes associated with the $a^-a^-c^0$ and $a^0a^0c^+$ rotations in Glazer's notation [48] and the bond disproportionation distortion B_{oc} extracted from a symmetry mode analysis with respect to a high symmetry Pm-$3m$ cubic cell.

Due to the lack of experimental bulk data (resulting from difficult in synthesizing the bulk nickelates), we cannot directly compare our DFT results to experimental data of insulating $SmNiO_3$. To the best of our knowledge, structural data are only available in the high temperature metallic orthorhombic symmetry [49], but the extracted lattice parameters ($a = 5.4328$ Å, $b = 5.3269$ Å, $c = 7.5648$ Å) or amplitude of octahedra rotations (0.4546 Å/f.u. and 0.6608 Å/f.u. for the $a^-a^-c^0$ and $a^0a^0c^+$ rotations, respectively) are compatible with our DFT parameters. The stabilization of the monoclinic phase $P2_1/n$ phase at low temperature is established in many other nickelates such as $NdNiO_3$ [50] or $YNiO_3$ [49] and is associated with a sizable breathing mode B_{oc} (see Table I) that splits the Ni cations into two inequivalent cations in the unit cell. Consequently, we identify a Ni$_L$ cation that sits in large O_6 octahedra and bears a magnetic moment larger than 1 ($\mu_{NiL} = 1.34\,\mu_B$) while the other Ni$_S$ cation is at the center of a compressed O_6 octahedra and has no magnetic moment. This is compatible with the disproportionation of Ni^{3+} cations to Ni_L^{2+} ($t_{2g}^6e_g^2$) and Ni_S^{4+} ($t_{2g}^6e_g^0$) cations, which are located in large (Ni$_L$) and compressed (Ni$_S$) octahedra, respectively. This results in a rocksalt pattern of $2+/4+$ cations [see Fig. 1(a)].

As inferred by the density of states projected on all O p states as well as on Ni$_L$ and Ni$_S$ d states reported in Fig. 2, the SCAN functional yields an insulating ground state with a band gap E_g of 0.90 eV. This is consistent with the insulating character of bulk $SmNiO_3$ [51] and with the experimental optical band gap estimated around 0.5 eV in Ref. [20] for $SmNiO_3$ thin films grown on $LaALO_3$, although strain may reduce the band gap amplitude [2,52]. The band gap is formed between a "split-off" occupied band of mainly hybridized Ni_L^{2+} e_g and O p states and unoccupied Ni_S^{4+} e_g states and O p states (Fig. 2). The situation is consistent with resonant inelastic x-ray spectroscopy measurements in $NdNiO_3$ [13] showing the existence of ligand holes in the materials, i.e., unoccupied O p states. It follows that hole doping might preferably—if possible—localize (form) a polaron (an acceptor state) with a Ni_L^{2+} character, while electron doping might preferably localize (form) a polaron (a donor state) having a Ni_S^{4+} character.

B. Ability to form polarons and localized states in the band gap

We now turn our attention to polaron formation upon hole and electron doping in $SmNiO_3$. We have first substituted one Sm^{3+} cation by a Ca^{2+} or Ce^{4+} cation, yielding a hole or electron doping level of 6.25%, respectively. The extra hole or electron is initially located to a precise Ni cation in the vicinity of the Ca/Ce introduced in the material, by forcing orbital occupancies. In order to avoid any assumption on the localization of the polaron, we have performed the test on the two types of Ni cations (i.e., either Ni$_L$ or Ni$_S$) in the material for both electron and hole doping. We find that a polaron is stabilized in our ground states producing a localized intermediate state in the band gap located at $\delta E = 0.10$ eV above the

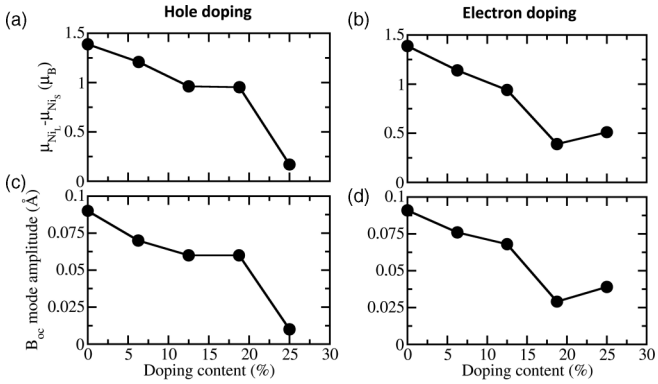

FIG. 4. Trends in (a) magnetic moment asymmetry of Ni cations (in μ_B) and (b) breathing distortion (in Å) as a function of the doping content (in %).

top of the valence band (i.e., an acceptor state) for hole doping or a localized intermediate state at $\delta E = 0.14$ eV below the bottom of the conduction band for electron doping, as shown in Figs. 3(a) and 3(b). At the same time, the material still develops a rather large gap E_g of 0.60 and 0.66 eV between the top of the valence and the bottom of the conduction band for hole and electron doping, respectively.

The polaron stabilization can be appreciated by the partial charge density maps associated with the intermediate states observed for hole and electron doping [Figs. 3(c) and 3(d)]. In both cases, we get that the polaron has an e_g symmetry and the added hole or electron is located in a d_y^2 and d_x^2 orbital, respectively. As one may have anticipated, a polaron for hole (electron) doping is formed only on Ni_L^{2+} (Ni_S^{4+}) sites in our DFT simulations. An initially nudged hole (electron) on a Ni_S (Ni_L) cation is not stable and the solution goes back to a band theory solution with no polaron stabilized. As suggested by the density of states, some tails do exist on neighboring Ni sites but with a negligible contribution for both hole and electron doping. The localization of holes and electrons in d_x^2 or d_y^2 orbitals is accompanied by a Jahn-Teller-like motion that accommodates the "orbital shape" of the spin-polarized singly occupied "e_g-like" state, with an asymmetry of Ni_L-O (Ni_S-O) bond length in the (*ab*) plane of 2.00/1.92 Å for hole (electron) doping.

The modification of the electronic structure upon doping is confirmed by the computed magnetic moments. Through hole (electron) doping, the Ni_L (Ni_S) cation holding the polaron now exhibits a magnetic moment of 0.87 μ_B (1.04 μ_B) with SCAN functional, compatible with a 3+ formal oxidation state, i.e., in a nondisproportionated state. At the same time, the modification of Ni magnetic moments induces an asymmetry of the spin-polarized potential experienced by each Ni_S and Ni_L element. It results in small variations of the surrounding spins amplitude, either on the Ni_S or Ni_L cation, with the magnetic moment of Ni_S cations not necessarily being exactly zero. We note that by looking at sphere integrated charges at the different Ni sites, we do not observe significant deviation of the total Ni *d* occupancies between doped and undoped materials—the largest difference of 0.08 electron is reached for the Ni_L or Ni_S site holding the polaron. This fact comes from a charge self-regulation mechanism [53] in which the electronic density around transition metals reorganizes itself in order to preserve the total number of *d* electrons on the TM (i.e., eight electrons for Ni cations).

C. Trends in hole and electron doping

Having established the ability of polaron formation, we have next performed a systematic study of electronic and structural properties upon hole and electron doping up to 25%. We report in Appendix B the key structural parameters of the optimized structures, that as we expected all adopt a *P*1

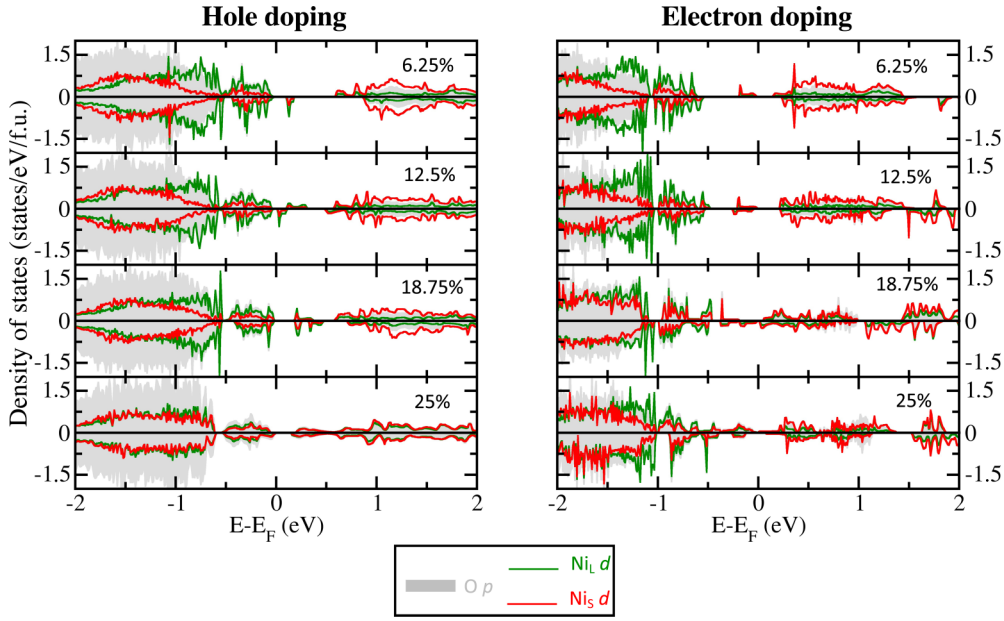

FIG. 5. Projected density of states (states/eV/f.u.) on O *p* states (filled grey), Ni_L *d* (green line), and Ni_S *d* (red line) as a function of hole (left panel) and electron (right) doping content. The 0 energy is set to the Fermi level E_F at 0 K, thus at the top of valence band for hole doping and top of donor states for electron doping.

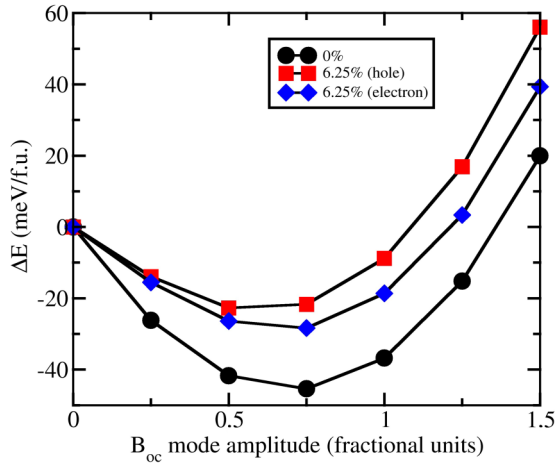

FIG. 6. Potential energy surface (in meV/f.u.) as a function of a breathing mode amplitude (in fractional units) condensed in a high symmetry cubic cell as function of doping content. An amplitude of 1 corresponds to the amplitude appearing in the pristine material ground state.

symmetry. Because disproportionation effects are responsible for the metal to insulator transition (MIT) in rare-earth nickelates [6,7,11,14], we first focus on the asymmetry of magnetic moments between Ni_L and Ni_S sites—associated with the formal oxidation state disproportionation in the bulk MIT—and on the amplitude of the breathing mode distortion B_{oc}—associated with the resulting bond disproportionation. Trends upon doping are reported in Fig. 4. The asymmetry of the magnetic moment between the two Ni cations existing in the pristine compound diminishes upon hole and electron doping, indicating a loss of charge disproportionation [Figs. 4(a) and 4(b)]. This is confirmed by the dependence of the breathing mode B_{oc} amplitude upon doping reported in Figs. 4(c) and 4(d) that follows a similar trend. Nevertheless, an unexpected feature for the electron doping should be highlighted: while the disproportionation totally vanishes at 25% of hole doping, it seems to slightly strengthen again at 25% for electron doping. As inferred by the lattice mode amplitude presented in Appendix B, we observe that the octahedra rotations strengthen a bit at 25% of electron doping. Due to the coupling of the breathing mode B_{oc} with these rotations [6]—large rotations favor the appearance of B_{oc} in bulk nickelates—this can explain the slight increase of the breathing mode we observe here. Nevertheless, the bulk "up-0-down-0" spin chains are suppressed by the 25% electron doping, whereas the "up-0-down-0" spin chains are less affected by the presence of hole doping, and we cannot rule out the possibility that the loss of the magnetic order affects the stabilization of B_{oc}. More complex magnetic solutions such as paramagnetism may be required to study such doping content.

To gain insight into the electronic properties, we report in Fig. 5 the density of states projected on O p as well as on Ni_L and Ni_S d states for increasing doping levels. We observe that the intermediate localized states spread more and more inside the gap as the substitution of cation A increases until they merge with the initial valence/conduction band, ultimately resulting in metallic states at 25% of Sm site substitutions with Ca or Ce. Nevertheless, there is a slight difference between hole and electron doping: hole doping likely results in a semiconducting state at 18.75% with a band gap of 0.15 eV, while electron doping already yields a metal. Finally at 25% of electron doping, we do not have any gap in the compound as shown by the projected density of states, and thus the breathing mode distortion estimated in this case may not be associated with the breathing mode resulting in the insulating state in the bulk compound. Similar results are observed with the PBEsol + U functional (see Appendix C).

D. Role of electron and hole doping on the electronic instability yielding disproportionation effect and the insulating phase of nickelates

As it is now accepted in the community [6,7,11,14,29], the breathing mode distortion B_{oc} is connected to the metal-insulator transition in bulk nickelates. This mode is associated with an electronic instability of the Ni +3 formal oxidation state in the bulk nickelates that will to disproportionate to more stable 2+ and 4+ formal oxidation state. This electronic instability can be observed by plotting the potential energy surface as a function of the breathing mode B_{oc} starting from a high symmetry cubic cell with the AFM-S order (Fig. 6). In the undoped material, we observe a single well potential whose energy minimum is located at a nonzero amplitude of B_{oc}. This indicates an electronic instability yielding the disproportionation effects, with a Ni_L ion bearing a magnetic moment larger than one, while the Ni_S cation bears no magnetic moment (see Fig. 6, filled black circles). We have then checked the precise role of electron and hole doping in $SmNiO_3$ on this electronic instability by recomputing the potential energy surface. Unfortunately, due to the absence of octahedra rotations that usually help in localizing electrons in perovskites and the absence of a structural relaxation for localizing a polaron—as we did while seeking for the ground state, but we want here to access the sole B_{oc} mode contribution—we could not stabilize solutions for doping contents higher than 6.25% with the SCAN functional. We can nevertheless observe that, upon hole or electron doping (Fig. 6), the energy gain associated with the B_{oc} mode decreases with respect to the pristine material and the minimum is now located to lower values of B_{oc} for hole doping. Thus, it confirms that doping tends to progressively remove the electronic instability associated with the MIT—charge and bond disproportionation effects—and that from pure electronic effects, hole doping suppresses the disproportionation instability—and thus the MIT—more rapidly than electron doping.

IV. DISCUSSION

At low doping content (6.25%), DFT simulations performed with the SCAN functional predicts an insulating character, in agreement with experimental results for both hole and electron doping in $RNiO_3$ [24–26]. At larger doping content, we observe a gap closure with an asymmetry for electron and hole doping content, again compatible with the experimental results of Garcia-Muñoz *et al.* [24] and Xiang *et al.* [25]. Nevertheless, these experimental works reveal (i) a gap closure at lower doping and that (ii) electron doping has a weaker effect on the closure of the MIT than hole doping. Our DFT work predicts a slightly different picture with a higher

TABLE II. Atomic positions of the Sm cations in the supercell.

	x/a	y/b	z/c		x/a	y/b	z/c
Sm (1)	0.00	0.00	0.00	Sm (9)	0.25	0.50	0.00
Sm (2)	0.00	0.00	0.50	Sm (10	0.25	0.50	0.50
Sm (3)	0.50	0.00	0.00	Sm (11)	0.75	0.50	0.00
Sm (4)	0.50	0.00	0.50	Sm (12)	0.75	0.50	0.50
Sm (5)	0.50	0.00	0.25	Sm (13)	0.25	0.50	0.25
Sm (6)	0.50	0.00	0.75	Sm (14)	0.25	0.50	0.75
Sm (7)	0.00	0.00	0.25	Sm (15)	0.75	0.50	0.25
Sm (8)	0.00	0.00	0.75	Sm (16)	0.75	0.50	0.75

critical value for doping content before reaching the metallic state (up to 18.75%), and a higher hole carrier concentration with respect to electron carrier concentration before reaching a metal. These discrepancies might have several origins: (i) Xiang *et al.* [25] studied Ca doping in $SmNiO_3$ but in thin films, and we cannot rule out the possibility that strain affects the metal-insulator transition upon doping [54]; (ii) Garcia-Muñoz *et al.* [24] examined bulk materials but with alternative cations (Nd instead of Sm, Th instead of Ce) and steric effects may alter the critical values in the spirit of the MIT temperature in bulk $RNiO_3$; (iii) we have not modeled paramagnetism in our DFT simulations, although we expect that the low temperature, spin-ordered phase inherits the physics of the PM phase [7,29]; and (iv) one might use larger supercells in our DFT calculations in order to represent a more possible local motif for Ni cations (see Appendix A). Nevertheless, our results regarding the potential energy surfaces associated with the breathing distortion with doping suggest that hole doping suppresses the MIT more rapidly than electron doping. This is in agreement with the indirect experimental determination of the intrinsic electronic contribution to the MIT of Garcia-Muñoz *et al.* [24] —authors artificially removed the steric effect contribution to the MIT.

V. CONCLUSION

In conclusion, using DFT calculations, we simulated the effect of hole and electron doping in bulk $SmNiO_3$ by substituting Sm^{3+} by Ca^{2+} and Ce^{4+}, respectively, and studied the polaron formation. In particular, we showed that DFT, without any U parameter but with a functional better amending the self-interaction error inherent to DFT and capturing the band gap of the pristine material, produces a polaronic state in the band gap at low doping. This results in acceptor (hole doping) or donor (electron doping) states and a semiconducting behavior at moderate doping concentrations. As both hole and electron doping increases, the gap decreases and the bond disproportionation vanishes, until reaching a metallic state at large doping concentrations. Our results are globally in line with experimental reports for both bulk and thin films, which validates the use of DFT and of the meta-GGA SCAN functional in capturing doping effects in $RNiO_3$ materials. Therefore, these results validate the study of these compounds in the form of thin films by using DFT without U parameter and even extend the study to superconducting infinite-layer nickelates [55].

Data are available upon reasonable request to the authors.

TABLE III. Atomic positions of substituted Sm cations in the supercell for simulating the doping effects.

Doping content	Atoms	x/a	y/b	z/c
12.5%	Ca/Ce (1)	0.250	0.500	0.250
	Ca/Ce (2)	0.500	0.000	0.750
18.75%	Ca/Ce (1)	0.500	0.000	0.000
	Ca/Ce (2)	0.750	0.500	0.000
	Ca/Ce(3)	0.00	0.000	0.250
25%	Ca/Ce (1)	0.750	0.500	0.000
	Ca/Ce (2)	0.000	0.000	0.000
	Ca/Ce(3)	0.250	0.500	0.250
	Ca/Ce(4)	0.500	0.000	0.750

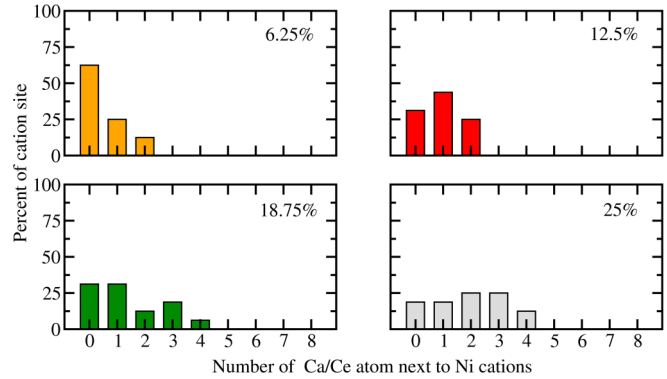

FIG. 7. Percent of Ni cations having 0–8 Ca/Ce neighbors for the different doping content.

Data are available upon reasonable request to the authors.

ACKNOWLEDGMENTS

We acknowledge access granted to HPC resources of Criann through Projects No. 2020005 and No. 2007013 and of Cines through the DARI Project No. A0080911453. Support from the French ANR Project No. "QUANTOP" is acknowledged.

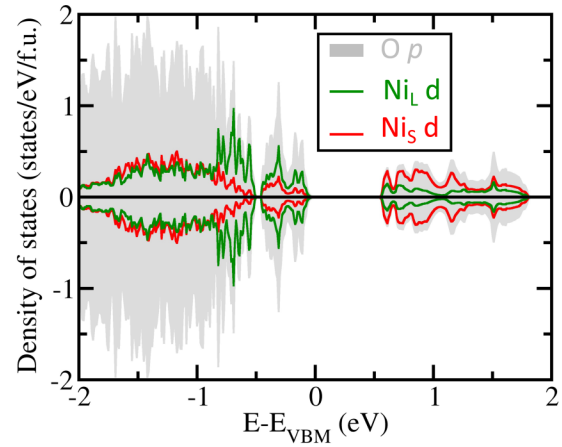

FIG. 8. Projected density of states (in states/eV/formula unit) on Ni_L d (green), Ni_S d (red), and O p (filled grey) states in the ground state structure of bulk $SmNiO_3$ using the PBEsol + U exchange correlation functional. The 0 energy is set at the valence band maximum.

TABLE IV. Structural parameters of hole doped nickelates.

% doping	a (Å)	b (Å)	c (Å)	$\alpha(^\circ)$	$\beta(^\circ)$	$\gamma(^\circ)$	B_{oc} (Å)	$a^-a^-c^0$ (Å)	$a^0a^0c^+$ (Å)
6.25	5.4040	5.2860	7.5150	90.0190	90.0700	89.7060	0.0740	0.6290	0.4500
12.5	5.3940	5.2980	7.4790	90.1230	89.9680	89.8960	0.0610	0.6270	0.4350
18.7	5.3870	5.3020	7.4520	90.1400	89.9960	90.2820	0.0560	0.6240	0.4300
25	5.3650	5.2940	7.4400	90.0180	90.0360	89.9420	0.0050	0.5970	0.4260

APPENDIX A: *A* SITE CATION POSITIONS IN THE SUPERCELL

We report in Table II the A site cation positions in the 16 formula units (f.u.) supercell tested in our simulations. For simplicity, these are provided in an undistorted supercell corresponding to a ($2\sqrt{2}a$, $\sqrt{2}a$, $4a$) cubic cell and A site cations are located at the corner of the primitive cubic cell.

For the 6.25% doping content, we simply substitute one Sm cation by a Ca or a Ce atom. We report in Table III the position of substituted atoms for 12.5%, 18.75%, and 25% of doping content.

We report in Fig. 7 the number of Ca/Ce cations in the vicinity of Ni cations in the doped materials, that can vary from 0 to 8. This reflects the occurrence of each local motif for Ni cations. While we should observe a distribution with a mode roughly centered on the percent of atom substituted times the number of neighbors for a perfectly disordered material (i.e., we expect that each Ni cation has 2 and 1 Ca/Ce atom in average in their vicinity for 25% and 12.5% of doping content, respectively), we see that our distributions of Ni motifs are reminiscent of these values, with peaked distributions between 0 and 1 for 6.25%, 1 at 12.5%, and around 2 for 25% of doping content. Nevertheless, these distributions may be improved, notably at low doping content, by using larger supercells that would allow more local motifs for the Ni cations.

APPENDIX B: OPTIMIZED PARAMETERS OF THE DOPED MATERIALS

We report in Tables IV and V the optimized lattice parameters of our hole and electron doped materials, respectively, as well as the amplitude associated with the octahedra rotations ($a^-a^-c^0$ and $a^0a^0c^+$) and breathing mode distortion B_{oc}. In all cases, the space group is found to be $P1$ (no symmetry at all).

APPENDIX C: DOPING EFFECTS IN $SmNiO_3$ WITH THE PBEsol + U FUNCTIONAL

Along with the SCAN functional, we have also performed DFT simulations with the PBEsol [56] + U [57] functional with $U = 2$ eV as in Ref. [8]. Regarding the bulk properties, we end up with very similar results to the SCAN functional at the exception that the band gap is found smaller ($E_g = 0.54$ eV) as shown by Fig. 8.

We report in Fig. 9 the projected density of states upon hole and electron doping in $SmNiO_3$ using the PBEsol + U functional. Results are similar to the SCAN functional, although the estimated gaps upon doping are smaller than the SCAN gaps, a situation similar to the results obtained for the bulk material. A semiconducting state is still obtained up to 18.75% (12.5%) of hole (electron) doping.

TABLE V. Structural parameters of electron doped nickelates.

% doping	a (Å)	b (Å)	c (Å)	$\alpha(^\circ)$	$\beta(^\circ)$	$\gamma(^\circ)$	B_{oc} (Å)	$a^-a^-c^0$ (Å)	$a^0a^0c^+$ (Å)
6.25	5.4280	5.2890	7.5390	90.0320	89.9690	89.8630	0.0760	0.6580	0.4660
12.5	5.4620	5.2770	7.5420	90.1080	89.9660	90.2450	0.0680	0.6730	0.4910
18.7	5.4570	5.2720	7.5690	90.1340	89.9230	90.0100	0.0260	0.6850	0.4920
25	5.5380	5.2600	7.5220	89.9900	90.0870	89.9270	0.0380	0.7070	0.5400

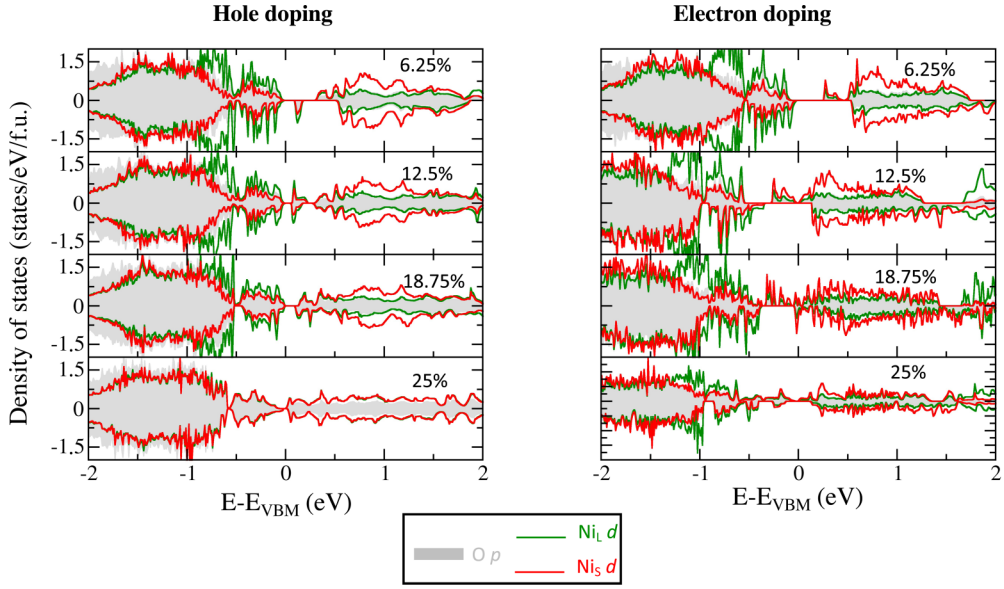

FIG. 9. Projected density of states (states/eV/f.u.) on O p states (filled grey), Ni$_L$ d (green line), and Ni$_S$ d (red line) as a function of hole (left panel) and electron (right) doping content. The 0 energy is set at the top of valence bands for both doping.

[1] P. Zubko, S. Gariglio, M. Gabay, P. Ghosez, and J.-M. Triscone, Annu. Rev. Condens. Matter Phys. **2**, 141 (2011).

[2] S. Catalano, M. Gibert, J. Fowlie, J. Iñiguez, J. M. Triscone, and J. Kreisel, Rep. Prog. Phys. **81**, 046501 (2018).

[3] G. Catalan, Phase Transit. **81**, 729 (2008).

[4] G. Giovannetti, S. Kumar, D. Khomskii, S. Picozzi, and J. van den Brink, Phys. Rev. Lett. **103**, 156401 (2009).

[5] J. Chaloupka and G. Khaliullin, Phys. Rev. Lett. **100**, 016404 (2008).

[6] A. Mercy, J. Bieder, J. Íñiguez, and P. Ghosez, Nat. Commun. **8**, 1677 (2017).

[7] J. Varignon, M. Bibes, and A. Zunger, Nat. Commun. **10**, 1658 (2019).

[8] J. Varignon, M. N. Grisolia, J. Íñiguez, A. Barthélémy, and M. Bibes, Npj Quantum Mater. **2**, 21 (2017).

[9] Z. Liao, N. Gauquelin, R. J. Green, K. Müller-Caspary, I. Lobato, L. Li, S. Van Aert, J. Verbeeck, M. Huijben, M. N. Grisolia, V. Rouco, R. El Hage, J. E. Villegas, A. Mercy, M. Bibes, P. Ghosez, G. A. Sawatzky, G. Rijnders, and G. Koster, Proc. Natl. Acad. Sci. **115**, E10284 (2018).

[10] A. Subedi, O. E. Peil, and A. Georges, Phys. Rev. B **91**, 075128 (2015).

[11] H. Park, A. J. Millis, and C. A. Marianetti, Phys. Rev. Lett. **109**, 156402 (2012).

[12] V. M. Goldschmidt, Naturwissenschaften **14**, 477 (1926).

[13] V. Bisogni, S. Catalano, R. J. Green, M. Gibert, R. Scherwitzl, Y. Huang, V. N. Strocov, P. Zubko, S. Balandeh, J. M. Triscone, G. Sawatzky, and T. Schmitt, Nat. Commun. **7**, 13017 (2016).

[14] G. M. Dalpian, Q. Liu, J. Varignon, M. Bibes, and A. Zunger, Phys. Rev. B **98**, 075135 (2018).

[15] M. Osada, B. Y. Wang, B. H. Goodge, K. Lee, H. Yoon, K. Sakuma, D. Li, M. Miura, L. F. Kourkoutis, H. Y. Hwang, M. Osada, and H. Y. Hwang, Nano Lett. **20**, 5735 (2020).

[16] D. Li, K. Lee, B. Y. Wang, M. Osada, S. Crossley, H. R. Lee, Y. Cui, Y. Hikita, and H. Y. Hwang, Nature (London) **572**, 624 (2019).

[17] A. S. Botana, F. Bernardini, and A. Cano, JETP **132**, 618 (2021).

[18] J. Shi, Y. Zhou, and S. Ramanathan, Nat. Commun. **5**, 4860 (2014).

[19] M. Kotiuga and K. M. Rabe, Phys. Rev. Mater. **3**, 115002 (2019).

[20] M. Kotiuga, Z. Zhang, J. Li, F. Rodolakis, H. Zhou, R. Sutarto, F. He, Q. Wang, Y. Sun, Y. Wang, N. A. Aghamiri, S. B. Hancock, L. P. Rokhinson, D. P. Landau, Y. Abate, J. W. Freeland, R. Comin, S. Ramanathan, and K. M. Rabe, Proc. Natl. Acad. Sci. USA **116**, 21992 (2019).

[21] P. Yoo and P. Liao, Phys. Chem. Chem. Phys. **22**, 6888 (2020).

[22] Q. Liu, G. M. Dalpian, and A. Zunger, Phys. Rev. Lett. **122**, 106403 (2019).

[23] J. Chen, W. Mao, B. Ge, J. Wang, X. Ke, V. Wang, Y. Wang, M. Döbeli, W. Geng, H. Matsuzaki, J. Shi, and Y. Jiang, Nat. Commun. **10**, 694 (2019).

[24] J. L. García-Muñoz, M. Suaaidi, M. J. Martínez-Lope, and J. A. Alonso, Phys. Rev. B **52**, 13563 (1995).

[25] P. H. Xiang, S. Asanuma, H. Yamada, I. H. Inoue, H. Akoh, and A. Sawa, Appl. Phys. Lett. **97**, 032114 (2010).

[26] I. Vobornik, L. Perfetti, M. Zacchigna, M. Grioni, G. Margaritondo, J. Mesot, M. Medarde, and P. Lacorre, Phys. Rev. B **60**, R8426 (1999).

[27] S. Zeng, C. S. Tang, X. Yin, C. Li, M. Li, Z. Huang, J. Hu, W. Liu, G. J. Omar, H. Jani, Z. S. Lim, K. Han, D. Wan, P. Yang, S. J. Pennycook, A. T. S. Wee, and A. Ariando, Phys. Rev. Lett. **125**, 147003 (2020).

[28] J. Sun, A. Ruzsinszky, and J. P. Perdew, Phys. Rev. Lett. **115**, 036402 (2015).

[29] J. Varignon, M. Bibes, and A. Zunger, Phys. Rev. B **100**, 035119 (2019).
[30] J. W. Furness, Y. Zhang, C. Lane, I. G. Buda, B. Barbiellini, R. S. Markiewicz, A. Bansil, and J. Sun, Commun. Phys. **1**, 11 (2018).
[31] C. Lane, J. W. Furness, I. G. Buda, Y. Zhang, R. S. Markiewicz, B. Barbiellini, J. Sun, and A. Bansil, Phys. Rev. B **98**, 125140 (2018).
[32] G. Kresse and J. Hafner, Phys. Rev. B **47**, 558 (1993).
[33] G. Kresse and J. Furthmüller, Comput. Mater. Sci. **6**, 15 (1996).
[34] P. E. Blöchl, Phys. Rev. B **50**, 17953 (1994).
[35] H. T. Stokes and D. M. Hatch, J. Appl. Crystallogr. **38**, 237 (2005).
[36] B. J. Campbell, H. T. Stokes, D. E. Tanner, and D. M. Hatch, J. Appl. Crystallogr. **39**, 607 (2006).
[37] J. Bieder, A. Mercy, W. Y. Tong, and P. Ghosez, Phys. Rev. B **102**, 081111(R) (2020).
[38] M. Coll, J. Fontcuberta, M. Althammer, M. Bibes, H. Boschker, A. Calleja, G. Cheng, M. Cuoco, R. Dittmann, B. Dkhil, I. El Baggari, M. Fanciulli, I. Fina, E. Fortunato, C. Frontera, S. Fujita, V. Garcia, S. T. B. Goennenwein, C. G. Granqvist, J. Grollier *et al.*, Appl. Surf. Sci. **482**, 1 (2019).
[39] J. P. Perdew, Int. J. Quantum Chem. **28**, 497 (1985).
[40] A. Seidl, A. Görling, P. Vogl, J. A. Majewski, and M. Levy, Phys. Rev. B **53**, 3764 (1996).
[41] J. P. Perdew, W. Yang, K. Burke, Z. Yang, E. K. U. Gross, M. Scheffler, G. E. Scuseria, T. M. Henderson, I. Y. Zhang, A. Ruzsinszky, H. Peng, J. Sun, E. Trushin, and A. Görling, Proc. Natl. Acad. Sci. USA **114**, 2801 (2017).
[42] C. Lane and J. X. Zhu, Phys. Rev. B **101**, 155135 (2020).
[43] J. Varignon, M. N. Grisolia, D. Preziosi, P. Ghosez, and M. Bibes, Phys. Rev. B **96**, 235106 (2017).
[44] J. Varignon, N. C. Bristowe, E. Bousquet, and P. Ghosez, Sci. Rep. **5**, 15364 (2015).
[45] A. Zunger, S.-H. Wei, L. G. Ferreira, and J. E. Bernard, Phys. Rev. Lett. **65**, 353 (1990).
[46] A. Van De Walle, P. Tiwary, M. De Jong, D. L. Olmsted, M. Asta, A. Dick, D. Shin, Y. Wang, L. Q. Chen, and Z. K. Liu, CALPHAD Comput. Coupling Phase Diagrams Thermochem. **42**, 13 (2013).
[47] J. P. Allen and G. W. Watson, Phys. Chem. Chem. Phys. **16**, 21016 (2014).
[48] A. M. Glazer, Acta Crystallogr., Sect. B: Struct. Crystallogr. Cryst. Chem. **28**, 3384 (1972).
[49] J. A. Alonso, M. J. Martínez-Lope, M. T. Casais, M. A. G. Aranda, and M. T. Fernández-Díaz, J. Am. Chem. Soc. **121**, 4754 (1999).
[50] J. L. García-Muñoz, M. A. G. Aranda, J. A. Alonso, and M. J. Martínez-Lope, Phys. Rev. B **79**, 134432 (2009).
[51] J. Pérez-Cacho, J. Blasco, J. García, M. Castro, and J. Stankiewicz, J. Phys.: Condens. Matter **11**, 405 (1999).
[52] F. Y. Bruno, K. Z. Rushchanskii, S. Valencia, Y. Dumont, C. Carrétéro, E. Jacquet, R. Abrudan, S. Blügel, M. Ležaić, M. Bibes, and A. Barthélémy, Phys. Rev. B **88**, 195108 (2013).
[53] H. Raebiger, S. Lany, and A. Zunger, Nature (London) **453**, 763 (2008).
[54] S. Catalano, M. Gibert, V. Bisogni, O. E. Peil, F. He, R. Sutarto, M. Viret, P. Zubko, R. Scherwitzl, A. Georges, G. A. Sawatzky, T. Schmitt, and J.-M. Triscone, APL Materials **2**, 116110 (2014).
[55] R. Zhang, C. Lane, B. Singh, J. Nokelainen, B. Barbiellini, R. S. Markiewicz, A. Bansil, and J. Sun, Comm. Phys. **4**, 118 (2021).
[56] J. P. Perdew, A. Ruzsinszky, G. I. Csonka, O. A. Vydrov, G. E. Scuseria, L. A. Constantin, X. Zhou, and K. Burke, Phys. Rev. Lett. **100**, 136406 (2008).
[57] S. L. Dudarev, G. A. Botton, S. Y. Savrasov, C. J. Humphreys, and A. P. Sutton, Phys. Rev. B **57**, 1505 (1998).